

Differential cross sections for the reactions $\gamma p \rightarrow p\eta$ and $\gamma p \rightarrow p\eta'$

M. Williams,^{1,*} Z. Krahn,^{1,†} D. Applegate,^{1,‡} M. Bellis,¹ C.A. Meyer,¹ K. P. Adhikari,²⁷ M. Anghinolfi,¹⁸ H. Baghdasaryan,^{36,27} J. Ball,⁷ M. Battaglieri,¹⁸ I. Bedlinskiy,²¹ B.L. Berman,¹⁴ A.S. Biselli,^{11,1} C. Bookwalter,¹³ W.J. Briscoe,¹⁴ W.K. Brooks,^{35,33} V.D. Burkert,³³ S.L. Careccia,²⁷ D.S. Carman,³³ P.L. Cole,¹⁶ P. Collins,³ V. Crede,¹³ A. D'Angelo,^{19,30} A. Daniel,²⁶ R. De Vita,¹⁸ E. De Sanctis,¹⁷ A. Deur,³³ B. Dey,¹ S. Dhamija,¹² R. Dickson,¹ C. Djalali,³² G.E. Dodge,²⁷ D. Doughty,^{8,33} M. Dugger,³ R. Dupre,² A. El Alaoui,^{20,§} L. Elouadrhiri,³³ P. Eugenio,¹³ S. Fegan,¹⁵ A. Fradi,²⁰ M.Y. Gabrielyan,¹² M. Garçon,⁷ G.P. Gilfoyle,²⁹ K.L. Giovanetti,²² F.X. Girod,^{7,¶} W. Gohn,⁹ E. Golovatch,³¹ R.W. Gothe,³² K.A. Griffioen,³⁷ M. Guidal,²⁰ N. Guler,²⁷ L. Guo,^{33,**} K. Hafidi,² H. Hakobyan,^{35,38} C. Hanretty,¹³ N. Hassall,¹⁵ K. Hicks,²⁶ M. Holtrop,²⁴ Y. Ilieva,^{32,14} D.G. Ireland,¹⁵ B.S. Ishkhanov,³¹ E.L. Isupov,³¹ S.S. Jawalkar,³⁷ H.S. Jo,²⁰ J.R. Johnstone,¹⁵ K. Joo,⁹ D. Keller,²⁶ M. Khandaker,²⁵ P. Khetarpal,²⁸ W. Kim,²³ A. Klein,^{27,**} F.J. Klein,⁶ V. Kubarovskiy,^{33,28} S.V. Kuleshov,^{35,21} V. Kuznetsov,²³ K. Livingston,¹⁵ H.Y. Lu,³² M. Mayer,²⁷ J. McAndrew,¹⁰ M.E. McCracken,¹ B. McKinnon,¹⁵ K. Mikhailov,²¹ T. Mineeva,⁹ M. Mirazita,¹⁷ V. Mokeev,^{31,33} K. Moriya,¹ B. Morrison,³ E. Munevar,¹⁴ P. Nadel-Turonski,⁶ C.S. Nepali,²⁷ S. Nicolai,²⁰ G. Niculescu,²² I. Niculescu,²² M.R. Niroula,²⁷ R.A. Niyazov,^{28,33} M. Osipenko,¹⁸ A.I. Ostrovidov,¹³ K. Park,^{32,23,¶} S. Park,¹³ E. Pasyuk,³ S. Anefalos Pereira,¹⁷ Y. Perrin,^{20,§} D. Pieschacon,¹⁶ S. Pisano,²⁰ O. Pogorelko,²¹ S. Pozdniakov,²¹ J.W. Price,⁴ S. Procureur,⁷ Y. Prok,^{36,††} D. Protopopescu,¹⁵ B.A. Raue,^{12,33} G. Ricco,¹⁸ M. Ripani,¹⁸ B.G. Ritchie,³ G. Rosner,¹⁵ P. Rossi,¹⁷ F. Sabatié,⁷ M.S. Saini,¹³ J. Salamanca,¹⁶ C. Salgado,²⁵ D. Schott,¹² R.A. Schumacher,¹ H. Seraydaryan,²⁷ Y.G. Sharabian,³³ E.S. Smith,³³ D.I. Sober,⁶ D. Sokhan,¹⁰ S.S. Stepanyan,²³ P. Stoler,²⁸ I.I. Strakovsky,¹⁴ S. Strauch,^{32,14} M. Taiuti,¹⁸ D.J. Tedeschi,³² S. Tkachenko,²⁷ M. Ungaro,^{9,28} M.F. Vineyard,³⁴ E. Voutier,^{20,§} D.P. Watts,^{15,‡‡} L.B. Weinstein,²⁷ D.P. Weygand,³³ M.H. Wood,^{5,32} J. Zhang,²⁷ and B. Zhao^{9,§§}

(The CLAS Collaboration)

¹Carnegie Mellon University, Pittsburgh, Pennsylvania 15213

²Argonne National Laboratory, Argonne, Illinois 60441

³Arizona State University, Tempe, Arizona 85287-1504

⁴California State University, Dominguez Hills, Carson, CA 90747

⁵Canisius College, Buffalo, NY 14208

⁶Catholic University of America, Washington, D.C. 20064

⁷CEA, Centre de Saclay, Irfu/Service de Physique Nucléaire, 91191 Gif-sur-Yvette, France

⁸Christopher Newport University, Newport News, Virginia 23606

⁹University of Connecticut, Storrs, Connecticut 06269

¹⁰Edinburgh University, Edinburgh EH9 3JZ, United Kingdom

¹¹Fairfield University, Fairfield CT 06824

¹²Florida International University, Miami, Florida 33199

¹³Florida State University, Tallahassee, Florida 32306

¹⁴The George Washington University, Washington, DC 20052

¹⁵University of Glasgow, Glasgow G12 8QQ, United Kingdom

¹⁶Idaho State University, Pocatello, Idaho 83209

¹⁷INFN, Laboratori Nazionali di Frascati, 00044 Frascati, Italy

¹⁸INFN, Sezione di Genova, 16146 Genova, Italy

¹⁹INFN, Sezione di Roma Tor Vergata, 00133 Rome, Italy

²⁰Institut de Physique Nucléaire ORSAY, Orsay, France

²¹Institute of Theoretical and Experimental Physics, Moscow, 117259, Russia

²²James Madison University, Harrisonburg, Virginia 22807

²³Kyungpook National University, Daegu 702-701, Republic of Korea

²⁴University of New Hampshire, Durham, New Hampshire 03824-3568

²⁵Norfolk State University, Norfolk, Virginia 23504

²⁶Ohio University, Athens, Ohio 45701

²⁷Old Dominion University, Norfolk, Virginia 23529

²⁸Rensselaer Polytechnic Institute, Troy, New York 12180-3590

²⁹University of Richmond, Richmond, Virginia 23173

³⁰Universita' di Roma Tor Vergata, 00133 Rome Italy

³¹Skobeltsyn Nuclear Physics Institute, Skobeltsyn Nuclear Physics Institute, 119899 Moscow, Russia

³²University of South Carolina, Columbia, South Carolina 29208

³³Thomas Jefferson National Accelerator Facility, Newport News, Virginia 23606

³⁴Union College, Schenectady, NY 12308

³⁵Universidad Técnica Federico Santa María, Casilla 110-V Valparaíso, Chile

³⁶University of Virginia, Charlottesville, Virginia 22901

³⁷College of William and Mary, Williamsburg, Virginia 23187-8795

³⁸Yerevan Physics Institute, 375036 Yerevan, Armenia

(Dated: August 14, 2019)

High-statistics differential cross sections for the reactions $\gamma p \rightarrow p\eta$ and $\gamma p \rightarrow p\eta'$ have been measured using the CLAS at Jefferson Lab for center-of-mass energies from near threshold up to 2.84 GeV. The η' results are the most precise to date and provide the largest energy and angular coverage. The η measurements extend the energy range of the world's large-angle results by approximately 300 MeV. These new data, in particular the η' measurements, are likely to help constrain the analyses being performed to search for new baryon resonance states.

PACS numbers: 11.80.Cr 11.80.Et 13.30.Eg 14.20.Gk

I. INTRODUCTION

Studying low-energy η and η' photoproduction presents an interesting opportunity to search for new baryon resonances. Since both of these mesons have isospin $I = 0$, the $N\eta$ and $N\eta'$ final states couple to N^* states but not Δ^* states. Previous experiments have produced precise cross section measurements for the $\gamma p \rightarrow p\eta$ reaction from threshold up to a center-of-mass energy, W , of approximately 2.5 GeV [1, 2, 3, 4]. For the $\gamma p \rightarrow p\eta'$ reaction, previous results are fairly precise from threshold up to $W \approx 2.2$ GeV [5].

Studies performed on these previous experimental data have yielded evidence for nucleon resonance contributions. For example, Anisovich *et al.* [6] confirmed that η photoproduction is dominated near threshold by contributions from the $S_{11}(1535)$ and $S_{11}(1650)$ states. Evidence was also found for contributions from other resonances at higher energies, along with strong t -channel contributions in the forward direction. The previously published CLAS η' results support contributions from several resonance states as well [5].

The η' results presented in this paper are more precise than any previous measurements and extend the large-angle energy range by approximately 600 MeV. They will provide stronger constraints on models that attempt to extract resonance contributions in this reaction. Our η measurements extend the energy range of the world's large-angle results by approximately 300 MeV. Significant discrepancies exist between our η results and those previously published by CB-ELSA [2] at higher energies (see Section VIII). These new results for both η and η'

will surely have an impact on the physics interpretation of these reactions.

II. EXPERIMENTAL SETUP

The data were obtained using the CEBAF Large Acceptance Spectrometer (CLAS) housed in Hall B at the Thomas Jefferson National Accelerator Facility in Newport News, Virginia. A 4 GeV electron beam hitting a 10^{-4} radiation length gold foil produced real photons via the bremsstrahlung process. The recoiling electrons were then analyzed using a dipole magnet and scintillator hodoscopes in order to obtain, or “tag”, the energy of the photons [7]. Photons in the energy range from 20% to 95% of the electron beam energy were tagged and thus measured with an energy resolution of 0.1% of the electron beam energy. The data were analyzed in center-of-mass energy bins that varied in width from 10 MeV up to 40 MeV, depending on the statistics.

The physics target, which was filled with liquid hydrogen, was a 40-cm long cylinder with a radius of 2 cm. Continuous monitoring of the temperature and pressure permitted determination of the density with uncertainty of 0.2%. The target cell was surrounded by 24 “start counter” scintillators that were used in the event trigger.

The CLAS detector utilized a non-uniform toroidal magnetic field of peak strength near 1.8 T in conjunction with drift chamber tracking to determine particle momenta. The detector was divided into six sectors, such that when viewed along the beam line it was six-fold symmetric. Charged particles with laboratory polar angles in the range $8^\circ - 140^\circ$ could be tracked over approximately 83% of the azimuthal angle. A set of 288 scintillators placed outside of the magnetic field region was used in the event trigger and during off-line analysis in order to determine time of flight (TOF) of charged particles. The momentum resolution of the detector was, on average, about 0.5%. Other components of the CLAS, such as the Cerenkov counters and the electromagnetic calorimeters, were not used in this analysis. A more detailed description of the CLAS can be found in reference [8].

The events were collected using a “two-track” trigger. This trigger required a coincidence between signals from the photon tagger and the CLAS. The signal from the tagger consisted of an OR of 40 of the 61 timing scintil-

*Current address: Imperial College London, London SW7 2AZ, UK

†Current address: University of Minnesota, Minneapolis, MN 55455

‡Current address: Stanford University, Stanford, CA 94305

§Current address: LPSC-Grenoble, France

¶Current address: Thomas Jefferson National Accelerator Facility, Newport News, VA 23606

**Current address: Los Alamos National Laboratory, NM

††Current address: Christopher Newport University, Newport News, VA 23606

‡‡Current address: Edinburgh University, Edinburgh EH9 3JZ, UK

§§Current address: College of William and Mary, Williamsburg, VA 23187-8795

lators, corresponding to photon energies above 1.58 GeV. This run setup where only part of the tagger was included in the trigger was intended to mainly detect photons above 1.58 GeV, avoiding the large bremsstrahlung contribution from photons of lower energy. However, events originating from a photon of energy below 1.58 GeV (corresponding to a hit in counters 41-61) were recorded when they had an accidental (random) hit in one of the triggered tagger counters. By using these “accidental” events, we were able to collect data for photons with energies from ~ 1 GeV to 1.58 GeV. This required applying an appropriate renormalization based on the probability for such a random coincidence to occur (see Sec. VI). The signal from the CLAS required at least two sector-based signals. These signals consisted of an OR of any of the 4 start counter scintillators in coincidence with an OR of any of the 48 time-of-flight scintillators in the sector. The rate at which hadronic events were accumulated was about 5 kHz; however, only a small fraction of these events contained the reactions of interest to the analysis presented here.

III. DATA AND EVENT SELECTION

The data reported here were obtained in the summer of 2004 during the CLAS “g11a” data taking period, in which approximately 20 billion triggers were recorded. The relatively loose electronic trigger led to accumulation of data for a number of photoproduction reactions. During offline calibration, the timing of the photon tagger, the start counter and the time-of-flight elements were aligned with each other. Calibrations were also made for the drift times of each of the drift chamber packages and the pulse heights of each of the time-of-flight counters. Finally, processing of the raw data was performed in order to reconstruct tracks in the drift chambers and match them with time-of-flight counter hits.

The reconstructed tracks were corrected for small imperfections in the magnetic field map and drift chamber alignment, along with their mean energy losses as they passed through the target, the beam pipe, the start counter and air. In addition, small corrections were made to the incident photon energies to account for mechanical sag in the tagger hodoscope.

The CLAS was optimized for detection of charged particles; thus, the $\pi^+\pi^-\pi^0$ decay of the η and the $\pi^+\pi^-\eta$ decay of the η' were used to select the reactions of interest in this analysis. Detection of two positively charged particles and one negatively charged particle was required. A 1-constraint kinematic fit to the hypothesis $\gamma p \rightarrow p\pi^+\pi^-(\pi^0/\eta)$ was performed. This fit adjusts the momenta of all measured particles within their measurement errors such that energy and momentum are conserved and the missing mass is that of either a π^0 or an η . The shifts in the momentum, combined with the known errors, yields a χ^2 which is then converted to a probability (confidence level) that the event is the desired

reaction. A cut was placed on the resulting confidence levels in order to select events consistent with one of the two topologies. Fits were run for each of the possible p, π^+ particle identification assignments using each of the recorded photons in the event. Photon-particle combinations with confidence levels greater than 10% were retained for further analysis. The trial identity as a proton or a pion for positive particles (assigned by the kinematic fit) was then checked using time-of-flight and momentum measurements.

The covariance matrix of the measured momenta was studied using four-constraint kinematic fits performed on the exclusive reaction $\gamma p \rightarrow p\pi^+\pi^-$ in both real and Monte Carlo data samples. The confidence levels in all kinematic regions were found to be sufficiently flat and the pull-distributions (stretch functions) were Gaussians centered at zero with $\sigma = 1$ (see Fig. 1). The uncertainty in the extracted yields due to differences in signal lost because of this confidence-level cut in real as compared to Monte Carlo data is estimated to be about 3%.

All negatively charged tracks were assigned a π^- identification. For positively charged tracks, the trial identification from the kinematic fit was checked using time-of-flight and momentum measurements. The tagger signal time, which was synchronized with the accelerator radio-frequency (RF) timing, is used to obtain the start time for the event by accounting for the photon time of flight from the tagger to the reaction vertex. The stop time for each track was obtained from the TOF scintillator element hit by the track. The difference between these two times was the measured time of flight, t_{meas} . Track reconstruction through the CLAS magnetic field yielded both the momentum, \vec{p} , of each track, along with the path length, L , from the reaction vertex to the time-of-flight counter hit by the track. The expected time of flight for a mass hypothesis, m , is then given by

$$t_{exp} = \frac{L}{c} \sqrt{1 + \left(\frac{m}{p}\right)^2}. \quad (1)$$

The difference in these two time-of-flight calculations, $\Delta tof = t_{meas} - t_{exp}$, was used in order to separate protons from pions and to remove events associated with incorrect photons.

Figure 2 shows Δtof for tracks passing the kinematic fit under the π^+ hypothesis *vs.* Δtof for the track passing the fit under the proton hypothesis. The region near (0, 0) contains events where both tracks are good matches to their respective particle identification hypotheses. The 2 ns radio-frequency time structure of the accelerator is evident in the out-of-time event clusters. Events outside of the black lines, where neither hypothesis was met, were cut from our analysis. This cut was designed to remove a minimal amount of good events. The Feldman-Cousins method [9] was used to place an upper limit on the signal lost at 1.3%. Any remaining accidental events fell into the broad background under the η/η' , and were rejected during the signal-background separation stage of the analysis discussed in Section IV.

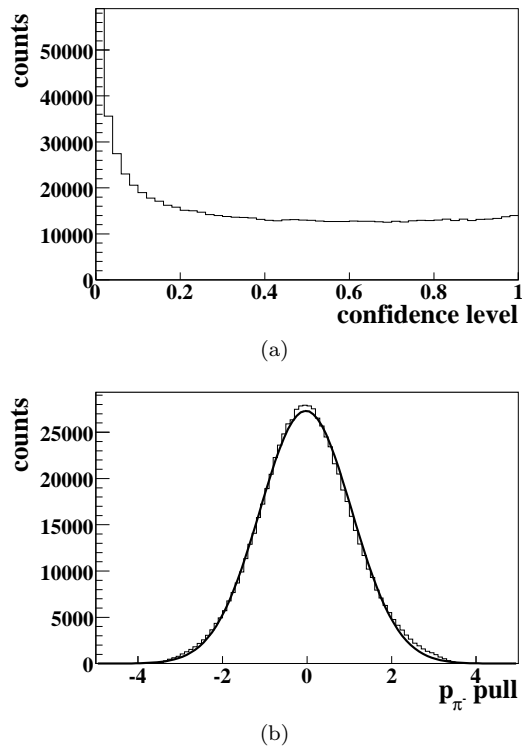


FIG. 1: (a) The confidence levels resulting from four-constraint kinematic fits performed on a sample of events to the calibration hypothesis $\gamma p \rightarrow p\pi^+\pi^-$ integrated over all kinematics. The “peak” near zero consists of events that do not match the hypothesis, along with poorly measured (due to multiple scattering, *etc.*) signal events. Agreement with the ideal (flat) distribution for signal events is very good. (b) Example pull-distribution for the momentum of the π^- from the same kinematic fits as in (a). Only events with a confidence level larger than 1% are shown. The line represents a Gaussian fit to this distribution. For this event sample, the parameters obtained are $\mu = -0.029 \pm 0.001$, $\sigma = 1.086 \pm 0.001$ (the uncertainties are purely statistical), which are in very good agreement with the ideal values $\mu = 0$, $\sigma = 1$. Both (a) and (b) are good indicators that the CLAS error matrix is well understood. We note that the 10% confidence-level cut used in the analysis corresponds to the relatively flat region of the confidence-level plot. (This figure is reproduced from reference [12]).

Fiducial cuts were applied on the momenta and angles of the tracks in order to select events from the well-understood regions of the detector. Included in these cuts was the removal of 13 of the 288 time-of-flight elements due to poor performance. In addition, events where the missing π^0 was moving along the beam line, $\cos \theta_{c.m.}^{\pi^0} > 0.99$, were cut in order to remove leakage from the $\gamma p \rightarrow p\pi^+\pi^-$ reaction (because of the very forward angle, the center-of-mass and lab angles are very similar, so a 0.99 cut in the center of mass corresponds to an even tighter cut in the lab frame). These arise from events in which two in-time photons occur where the higher-energy one is incorrectly associated with the charged tracks in

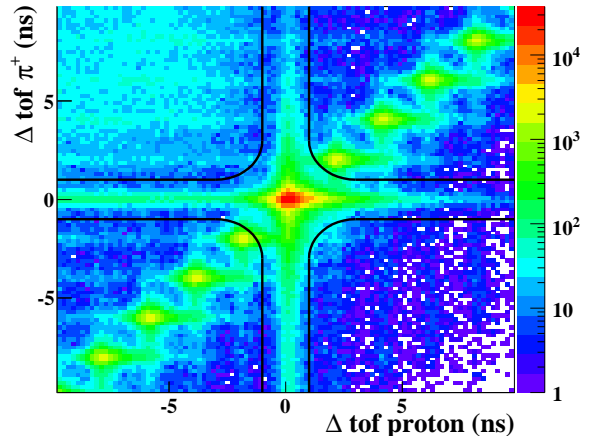


FIG. 2: (Color Online) Δtof_{π^+} (ns) vs. Δtof_p (ns): Particle identification cut for a sample of events that pass a 10% confidence level cut when kinematically fit to the hypothesis $\gamma p \rightarrow p\pi^+\pi^-$ (π^0). The black lines indicate the timing cuts. Note the logarithmic scale on the intensity axis.

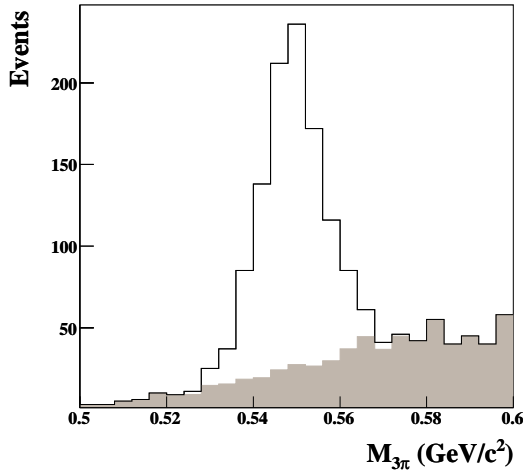
the event. The lower-energy photon causes the reaction $\gamma p \rightarrow p\pi^+\pi^-$. When the event is reconstructed using the higher energy photon, there appears to be excess energy and missing momentum along the photon direction. In some cases, this can be mis-reconstructed as a missing π^0 moving along the beam direction. Our cut at $\cos \theta_{c.m.}^{\pi^0} > 0.99$ removes these events. A more detailed description of the entire analysis procedure presented in this paper can be found in Ref. [10].

The resulting data have been sorted into bins in W . For the η , there are 76 bins from W of 1.570 GeV to 2.840 GeV. From 1.570 GeV to 2.100 GeV, the bins are 10 MeV wide. From $W = 2.100$ GeV to 2.360 GeV, the bins are 20 MeV wide. In the range from 2.360 GeV to 2.640 GeV, the bins are 40 MeV wide. Finally, there is a 50 MeV wide bin from $W = 2.680$ GeV to 2.730 GeV and a bin from 2.750 GeV to 2.840 GeV. The η' data are divided into 44 bins from $W = 1.900$ GeV up to 2.840 GeV. The bin widths for the η' are the same as those used for the η .

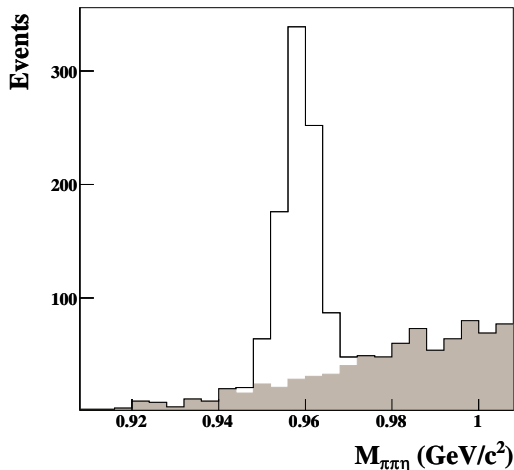
IV. SIGNAL-BACKGROUND SEPARATION

In order to extract physical observables from the η and η' photoproduction reactions studied here, it is necessary to separate background events from signal events. While such separation could be done via a simple sideband subtraction, our work on other reaction channels required the development of a more sophisticated event-based procedure. This event-based method, described in detail elsewhere [10, 11], was used to separate signal and background events.

The procedure takes advantage of the fact that in the invariant mass distributions, the signal is a narrow



(a)



(b)

FIG. 3: Example bins demonstrating signal-background separation. The plots are from the $W = 2.11$ GeV, $\cos \theta_{c.m.}^{\eta(\eta')} = 0.75$ kinematic bin for (a) η and (b) η' . The unshaded histograms are all of the data in each 4-MeV wide bin, while the shaded histograms are these same events weighted by the background factors, $1 - Q$. See text for details.

structure, while the background is relatively featureless. The key feature of the procedure involves selecting each event's n_c “nearest neighbor” events (we chose $n_c = 500$) using the quantity $\Delta \cos \theta_{c.m.}^{\eta(\eta')}$ as a distance metric between events. Each subset of n_c events occupies a very small region of phase space. Thus, the $M_{3\pi}(M_{\pi\pi\eta})$ distributions could safely be used to determine the probability of each event being a signal event—the event's Q -factor. The $M_{3\pi}/M_{\pi\pi\eta}$ distributions in each event's nearest neighbor event samples are fit to a narrow Gaussian (signal) plus a broad Gaussian and linear (background) function to determine the Q -factors. A few example invariant mass distributions are shown in Fig. 3. Note that such a distribution and fit are generated for each event in order to determine the Q -factor for the event. These

Q -factors are then used to weight each event's contribution to the fits that are in turn used to determine the detector acceptance. The Q -factors are also used to weight each event's contribution to the differential cross section.

Systematic studies were performed using different parametrizations of the background (including up to fourth order polynomials). From these studies, the systematic uncertainty in the yield extraction due to the choice of background shape is estimated to be 4.1% (3.1%) for the $\eta(\eta')$ analysis. The point-to-point uncertainties obtained from the individual fits varied depending on kinematics; however, it was typically about 4%–5%.

V. ACCEPTANCE

The typical method of computing a detector acceptance in a multi-particle final state such as those studied here is an iterative procedure to achieve a *physics model*. To determine if the model is good, one generates a Monte Carlo sample thrown according to the model. These events are then passed through an accurate detector simulation and the resulting event distributions are then compared to the physics distributions for the signal events as measured in the detector. After many iterations of the physics model, the two distributions should agree. At that point, one is able to use the physics model and the Monte Carlo sample to compute the detector acceptance.

There is an added complication to this procedure if there is background that is not easily separated from the signal. In such a case, one either needs to find a very clever way to effectively separate signal from background, or include the background events in the physics model. Generally, one is required to iterate the physics and background models until satisfactory agreement has been reached.

In this analysis, we have taken a more systematic approach to computing the acceptance. First, we have used the Q -factors discussed earlier to allow us to produce distributions of only signal events so that any model we use can ignore the background contribution. Second, we have used the fact that one can always expand any distribution in terms of partial waves. Thus our procedure involves determining a partial wave expansion (our physics model), which will make the weighted Monte Carlo data agree with the observed signal sample. This partial wave expansion can be used to weight phase space generated events such that the Monte Carlo and data distributions agree.

The efficiency of the detector was modeled using the standard CLAS GEANT-based simulation package and the Monte Carlo technique. A total of 100 million η and 80 million η' events were generated pseudo-randomly, sampled from a phase space distribution. Each particle was propagated from the event vertex through the CLAS resulting in a simulated set of detector signals for each track. The simulated events were then processed using

the same reconstruction software as the real data. In order to account for the event trigger used in this experiment (see Section II), a study was performed to obtain the probability of a track satisfying the sector-based coincidences required by the trigger as a function of kinematics and struck detector elements. The average effect of this correction in our analysis, which requires three detected particles, is about 5%–6%.

An additional momentum smearing algorithm was applied in order to better match the resolution of the Monte Carlo data to that of the real data. Its effects were studied using four-constraint kinematic fits performed on simulated $\gamma p \rightarrow p\pi^+\pi^-$ events. After applying the momentum smearing algorithm, the same covariance matrix used for the real data also produced flat confidence level distributions in all kinematic regions for the Monte Carlo data as well. The simulated η and η' events were then processed with the same analysis software as the real data, including the 1-constraint kinematic fits. At this stage, all detector and software efficiencies were accounted for.

In order to evaluate the CLAS acceptance for the reactions $\gamma p \rightarrow p\eta$ and $\gamma p \rightarrow p\eta'$, we chose to follow the same procedure that we used in obtaining the acceptance for ω photoproduction [12]. In this procedure, we expand the scattering amplitude for the pseudoscalar photoproduction, \mathcal{M} , in a very large basis of s -channel waves as follows:

$$\begin{aligned} \mathcal{M}_{m_i, m_\gamma, m_f}(\cos\theta_{c.m.}^{\eta(\eta')}, \vec{\alpha}) \\ \approx \sum_{J=\frac{1}{2}}^{\frac{11}{2}} \sum_{P=\pm} \mathcal{A}_{m_i, m_\gamma, m_f}^{JP}(\cos\theta_{c.m.}^{\eta(\eta')}, \vec{\alpha}), \end{aligned} \quad (2)$$

where $\vec{\alpha}$ denotes a vector of 34 fit parameters, m_i, m_γ, m_f are the target proton, incident photon and final proton spin projections on the incident photon direction in the center-of-mass frame, and \mathcal{A} are the s -channel partial wave amplitudes. The s -channel structure of the amplitudes, along with the details concerning the fit parameters are described in Ref. [10]. The amplitudes are evaluated using the `qft++` package [13].

Unbinned maximum likelihood fits were performed in each W bin to obtain the estimators $\hat{\alpha}$ for the parameters $\vec{\alpha}$ in Eq. (2). Background events were removed using the Q -factors directly in the fit as discussed in Refs. [10] and [11]. The results of these fits were used to obtain a physics weight, I_i , for each event. The weighted accepted Monte Carlo events fully reproduce the real data. An example comparison is shown in Figure 4 for one W bin of the η' data sample. The agreement between the weighted Monte Carlo and the data is very good. We note here that the results of these fits are not interpreted as physics, *i.e.* they are not considered evidence of resonance contributions to $\eta(\eta')$ photoproduction. They are simply used to provide a complete description of the data.

For a kinematic bin, the acceptance can be obtained

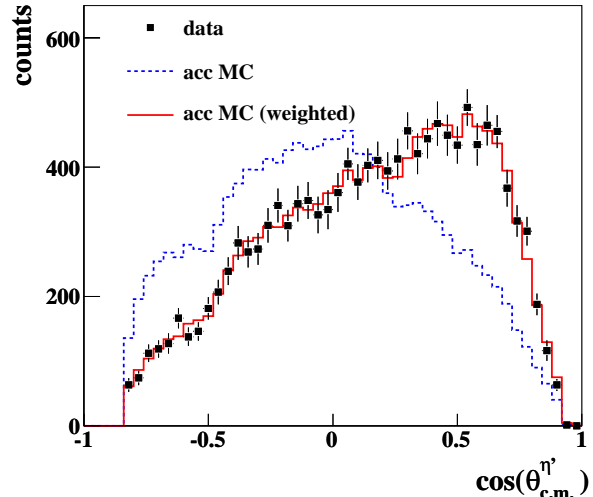


FIG. 4: (Color Online) An example fit result in a typical W bin for the η' photoproduction. The data are shown as black squares, the phase-space accepted Monte Carlo events are shown as the blue dashed line, while the weighted Monte Carlo events discussed in Section V are shown as the solid red curve. The weighted Monte Carlo provides an excellent description of the data.

as

$$acc(W, \cos\theta_{\eta, \eta'}) = \frac{\sum_i^{N_{acc}} I_i}{\sum_j^{N_{gen}} I_j}, \quad (3)$$

where $N_{acc}(N_{gen})$ are the number of accepted (generated) Monte Carlo events in the bin and the I 's are the event weights discussed above. An accurate physics generator would use the factors of I during the event generation stage, rather than weighting the events. The resulting acceptance calculation would be the same, modulo statistical fluctuations.

VI. NORMALIZATION

The measured rate of electrons detected by the tagger was used to compute the number of photons incident on the target by sampling tagger hits not in coincidence with the CLAS. These rates were integrated over the live-time of the experiment to obtain the total photon flux associated with each tagger element. Losses of photons in the beam line due to effects such as beam collimation were determined during dedicated runs using a total-absorption counter placed downstream of the CLAS [14].

The main method to calculate the experimental live-time during the “g11a” run was based on a clock. This live-time calculation was checked by using the counts of a Faraday cup located downstream of the detector. While

the Faraday cup is a standard device for electron beam intensity measurements, in this case it was counting many fewer events produced by interactions of the photon beam with the target. Consequently, the statistical error of this second live-time measurement was high. However, the Faraday-cup-based measurement allowed us to observe that at maximum electron beam current, the actual dead time was about a factor of two higher than that given by the clock-based measurement. The high statistical error of the Faraday-cup-based measurement led to an uncertainty in the absolute live-time measurement of about 3%.

As discussed in Section II, tagger counters 1-40 were in the trigger, while counters 41-61 were not. In order to have an event originating from a photon in the “untriggered” part of the tagger, the detector needed to record a random hit in one of the “triggered” counters during the trigger time window. The probability of such an occurrence can be calculated using the electron rates. For the data here, we found that the probability of this happening is 46.7%. This factor is then used to scale the flux in the untriggered counters.

Events in the $W = 1.955$ GeV bin span the boundary between tagger counters 40 and 41. Because events in this energy range arose from both triggered and untriggered counters, the flux in this bin was deemed unreliable. Thus, we report no cross sections for this energy. In addition to the above bin, the electronics in one of the tagger channels was not working properly during the run. This led to inaccurate flux measurements in the energy range $W = 2.73 - 2.75$ GeV. Differential cross sections will not be reported at these energies as well.

VII. SYSTEMATIC UNCERTAINTIES

An overall acceptance uncertainty of 5%–7%, depending on center-of-mass energy, was estimated for this analysis in Ref. [12]. This includes uncertainties due to particle identification (1.3%) and kinematic fitting confidence level cuts (3%), along with a relative acceptance uncertainty estimated by studying the agreement of physical observables obtained from each of the independent CLAS sectors (4 – 6%). The uncertainty on the normalization calculation was also estimated in Ref. [12] and found to be 7.9%. This includes contributions from photon transmission efficiency and live-time calculations.

The acceptance and normalization uncertainties discussed above were then combined with contributions from target density and length (0.2%), along with branching fraction (0.4% for the η , 1.5% for the η') to obtain a total uncertainty, excluding the point-to-point contributions from signal-background separation (from the fits), of about 9%–11%. The additional 4.1% and 3.1% global signal-background uncertainties discussed in Section IV must then be added in quadrature giving total uncertainties of about 10%–12% for both the η and η' . These errors are summarized in Table I.

Error	η	η'
Δ TOF Cut (PID)	1.3%	1.3%
Confidence Level Cut	3%	3%
Relative Acceptance	4%–6%	4%–6%
Normalization	7.9%	7.9%
Target Length	0.2%	0.2%
Branching Fraction	0.4%	1.5%
Background Shape	4.1%	3.1%
Total	10%–12%	

TABLE I: A summary of the systematic errors associated with these measurements. The total presents the range of values seen across all data bins.

VIII. RESULTS

For the differential cross section calculations, $d\sigma/d\Omega$, each center-of-mass energy bin was divided into 20 bins in $\cos\theta_{c.m.}^{\eta(\eta')}$ of width 0.1; however, results could not be extracted in every bin due to limitations in the detector acceptance. In total, 1082 η and 682 η' cross section points are reported. The centroid of each bin is reported as the mean of the range of the bin with non-zero acceptance. The results are shown in Figs. 5, 6, 7 and 8 and are available online in electronic form [15]. The error bars contain the uncertainties in the signal yield extraction (point-to-point signal-background separation uncertainties and statistical uncertainties in the number of signal events), along with statistical uncertainties from the Monte Carlo acceptance calculations. The global systematic uncertainties, discussed in Section VII, are estimated to be between 10%–12%, depending on center-of-mass energy.

Both data sets have a forward peak that becomes more prominent with increasing energy, most likely due to some t -channel exchange mechanism. Both data sets also have a backward peak at our highest energies, this could be indicative of u -channel contributions. There are other interesting features in the data sets which might be evidence for resonance production; however, a partial wave analysis would need to be performed to determine if this is the case. In the η photoproduction, the most prominent of these are a bump near $\cos\theta = 0.2$ in the low-energy data and a dip and a shoulder near $\cos\theta = -0.1$ in the 2.1 to 2.6 GeV region. For the η' there is a similar dip and shoulder.

Figure 9 shows a comparison of our η' results to previously published CLAS data [5]. The previous CLAS results were published using $\cos\theta_{c.m.}^{\eta'}$ bins of width 0.2, as opposed to the 0.1 width bins used in our work. To make this comparison, we have merged our bins (using a weighted average) to obtain the same binning as the previous CLAS results. The agreement is good with most data points agreeing within the error bars.

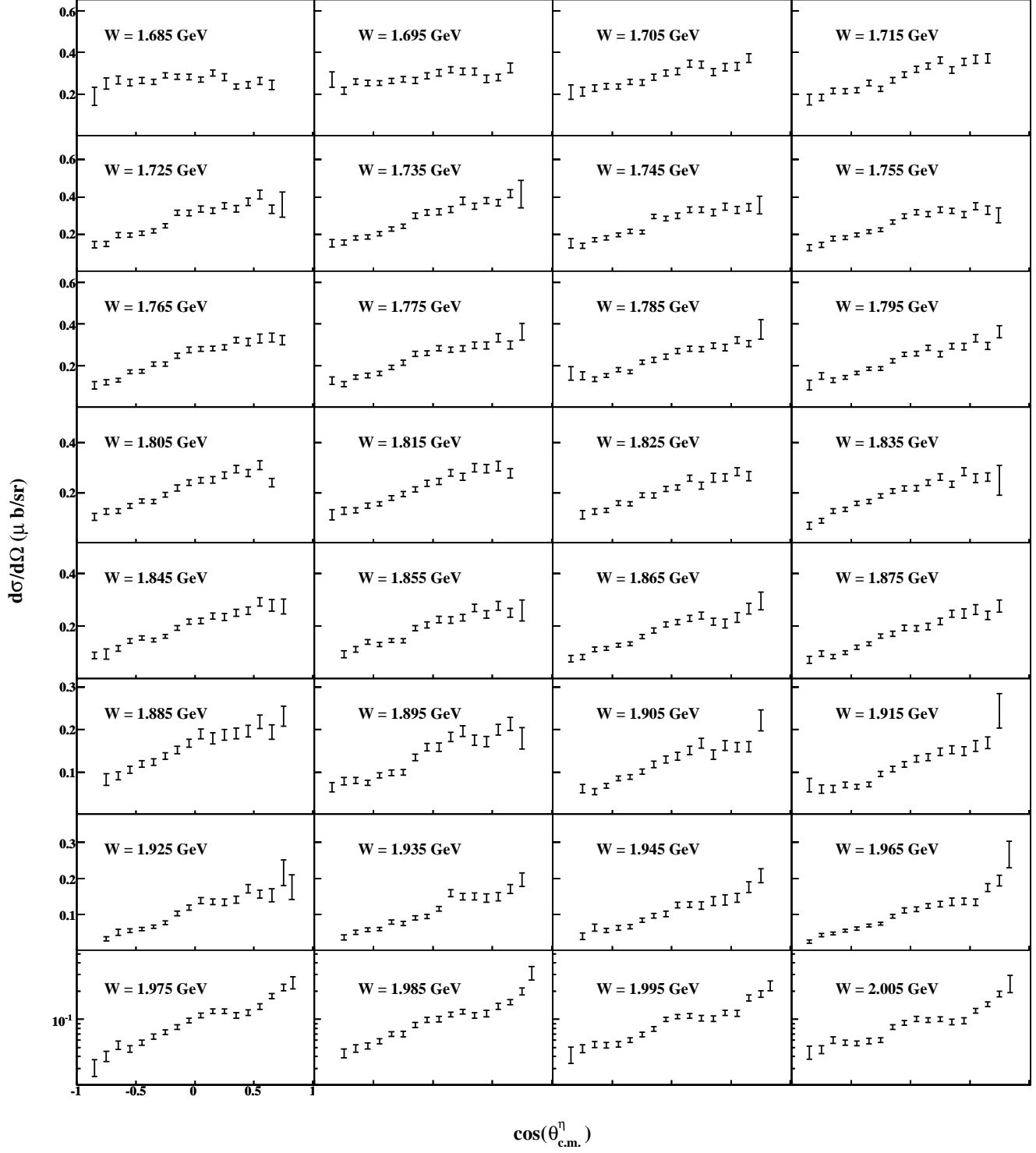


FIG. 5: $\frac{d\sigma}{d\Omega}$ ($\mu\text{b/sr}$) vs. $\cos\theta_{c.m.}^{\eta}$ for the $\gamma p \rightarrow p\eta$ reaction. Note that the vertical axis is linear for W up to 1.965 GeV and logarithmic above that.

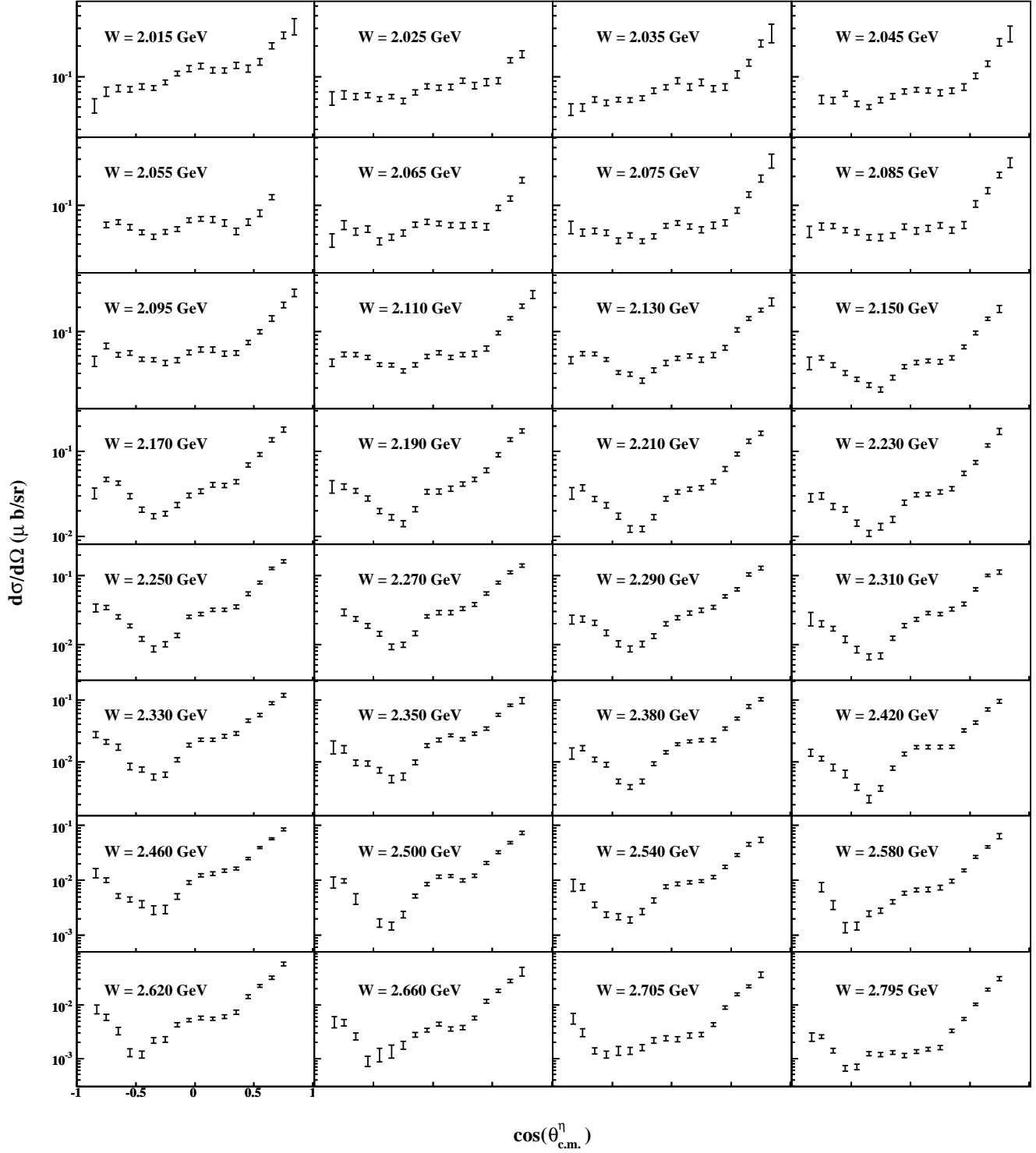


FIG. 6: $\frac{d\sigma}{d\Omega}(\mu\text{b/sr})$ vs. $\cos\theta_{\text{c.m.}}^\eta$ for the $\gamma p \rightarrow p\eta$ reaction. Note the logarithmic scale on the vertical axis.

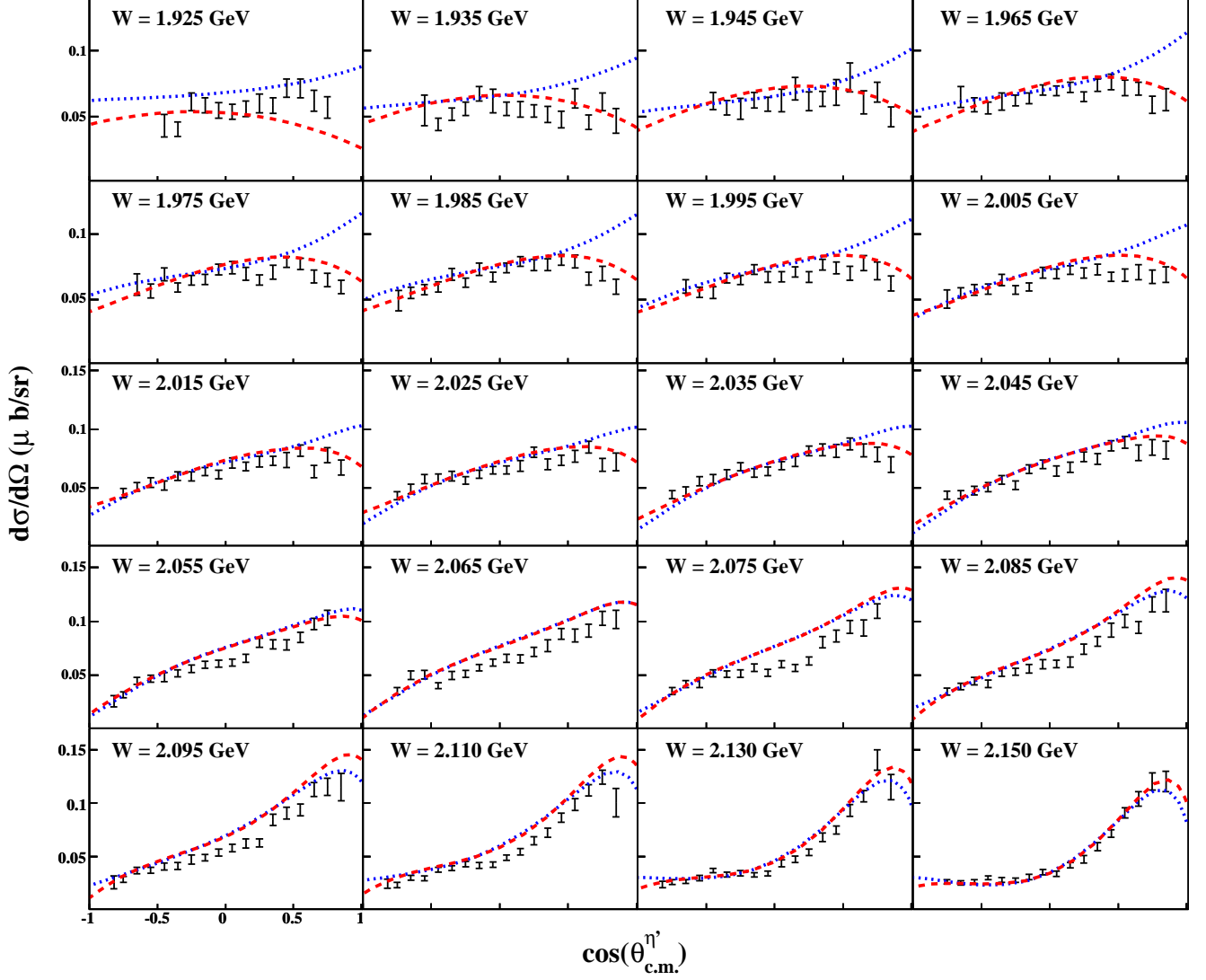


FIG. 7: $\frac{d\sigma}{d\Omega}$ ($\mu\text{b/sr}$) vs. $\cos\theta_{\text{c.m.}}^{\eta'}$ for the $\gamma p \rightarrow p\eta'$ reaction. Note that the vertical axis is linear. The (red) dashed line and (blue) dotted line are the results from Tabs. II and IV of Ref. [16], respectively.

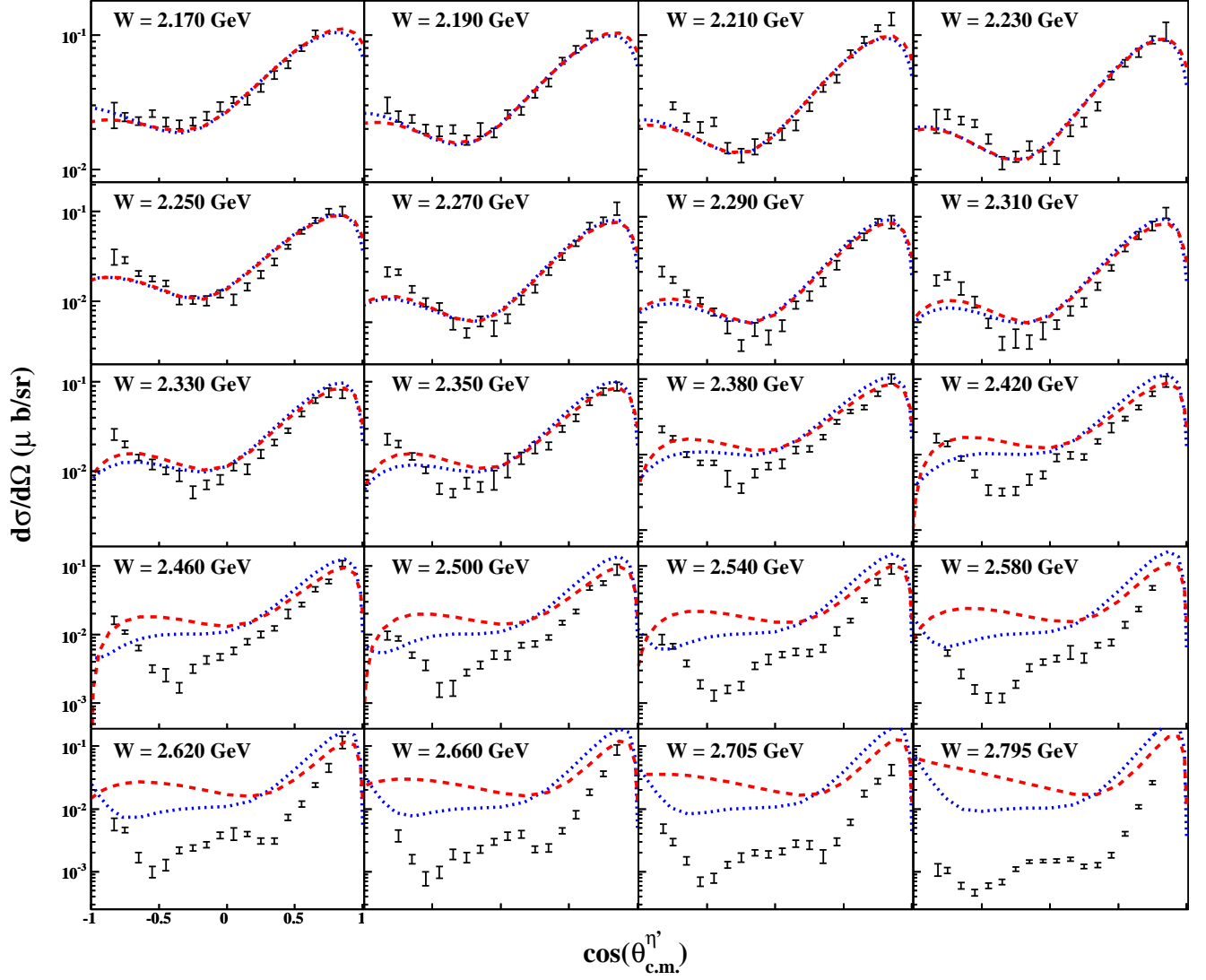


FIG. 8: $\frac{d\sigma}{d\Omega}$ ($\mu\text{b/sr}$) vs. $\cos\theta_{c.m.}^{\eta'}$ for the $\gamma p \rightarrow p\eta'$ reaction. Note that the vertical axis is logarithmic. The (red) dashed line and (blue) dotted line are the results from Tabs. II and IV of Ref. [16], respectively.

Figures 7 and 8 also shows the results from Tabs. II and IV of Ref. [16] (a relativistic meson-exchange model which includes various resonance contributions). Five versions of the model are presented in [16]; each fit to the previously published CLAS data [5]. The previous data were not able to distinguish between the five versions of the model. Near threshold, the Tab. II results clearly provide a better description of our data than those of Tab. IV. Given the poor performance of the models at higher energies, *i.e.* energies greater than what the models were fit to ($W > 2.25$ GeV), physics claims cannot be made from these models at this time. Our data, however, provide additional angular and energy coverage, along with increased precision, which should allow for more reliable extraction of resonance contributions to η' photoproduction by providing more stringent constraints on the models.

Figure 10 shows a comparison of our η results to published results from CLAS [1] and CB-ELSA [2]. The agreement between the three sets of measurements is fair to good at lower energies; however, at higher energies and forward angles large discrepancies begin to develop. The highest energy results reported by CB-ELSA are approximately four times larger than our measurements in the most forward angles. Even for $\cos\theta_{c.m.}^\eta \approx 0$, the CB-ELSA results are approximately two times larger than ours at these energies. The figure also shows a SAID fit [17] to the earlier data. Given the differences between our measurement and the earlier data, the poor agreement between the fit and our results is not surprising. Including our results into the fit will likely have a significant impact on the extracted physics.

This extremely large disagreement at higher energies and forward angles motivated us to extract the $\gamma p \rightarrow p\eta$ cross sections using an alternate procedure. This was carried out for points in our $W = 2.46$ GeV bin (which overlaps the second highest CB-ELSA bin). In this alternate procedure, we required the detection of only the $p\pi^+$, while ignoring the π^- . The η signal was then identified in the missing mass off the proton. This topology has both a very different acceptance and a significantly larger background than the one in which all three charged particles are detected; however, the results obtained for the two topologies were in excellent agreement (see Figure 11). This study, along with the fact that our results from this data set in several other channels (see Ref. [12] and [18]) are in good agreement with the world's data, has led us to conclude that it is very unlikely that there is some unknown acceptance or normalization issue present in our data.

We can offer no explanation as to why the CB-ELSA results differ so much from ours; however, the self-consistency of the results obtained from our data set,

using two distinct topologies, along with the high level of agreement with the world's data of cross sections extracted for other reactions from this same data set provide a high level of confidence in the results presented in this paper.

Ultimately, one expects that these data, combined with other measurements, will facilitate a large scale partial wave analysis that will be able to identify the baryon resonance contributions to these cross sections. While we did attempt to carry out single-channel partial wave analyses of both of these channels [19] (similar to that in Ref. [20]), the limited number of observables prevented us from drawing clear conclusions. Together with new measurements involving polarized beams and targets, these results should enable a deeper understanding of the nucleon resonances in the future.

IX. CONCLUSIONS

In summary, experimental results for η and η' photoproduction from the proton have been presented in the energy regime from near threshold up to $W = 2.84$ GeV. A total of 1082 η and 682 η' cross section points are reported. The η' results are the most precise to-date and provide the largest energy and angular coverage. The η measurements extend the energy range of the world's large-angle results by approximately 300 MeV. Unfortunately, discrepancies exist between the η results presented here and those previously published by CB-ELSA [2] at higher energies. We look forward to seeing the impact these new results will have on existing models of baryon photoproduction.

Acknowledgments

We thank Megan Friend for her valuable work on background subtraction studies for these reactions. We also thank the staff of the Accelerator and the Physics Divisions at Thomas Jefferson National Accelerator Facility who made this experiment possible. This work was supported in part by the U.S. Department of Energy (under grant No. DE-FG02-87ER40315), the National Science Foundation, the Italian Istituto Nazionale di Fisica Nucleare, the French Centre National de la Recherche Scientifique, the French Commissariat à l'Énergie Atomique, the Science and Technology Facilities Council (STFC), and the Korean Science and Engineering Foundation. The Southeastern Universities Research Association (SURA) operated Jefferson Lab under United States DOE contract DE-AC05-84ER40150 during this work.

[1] M. Dugger *et al.* [CLAS Collaboration], Phys. Rev. Lett. **89** 222002 (2002).

[2] V. Crede *et al.* [CB-ELSA Collaboration], Phys. Rev.

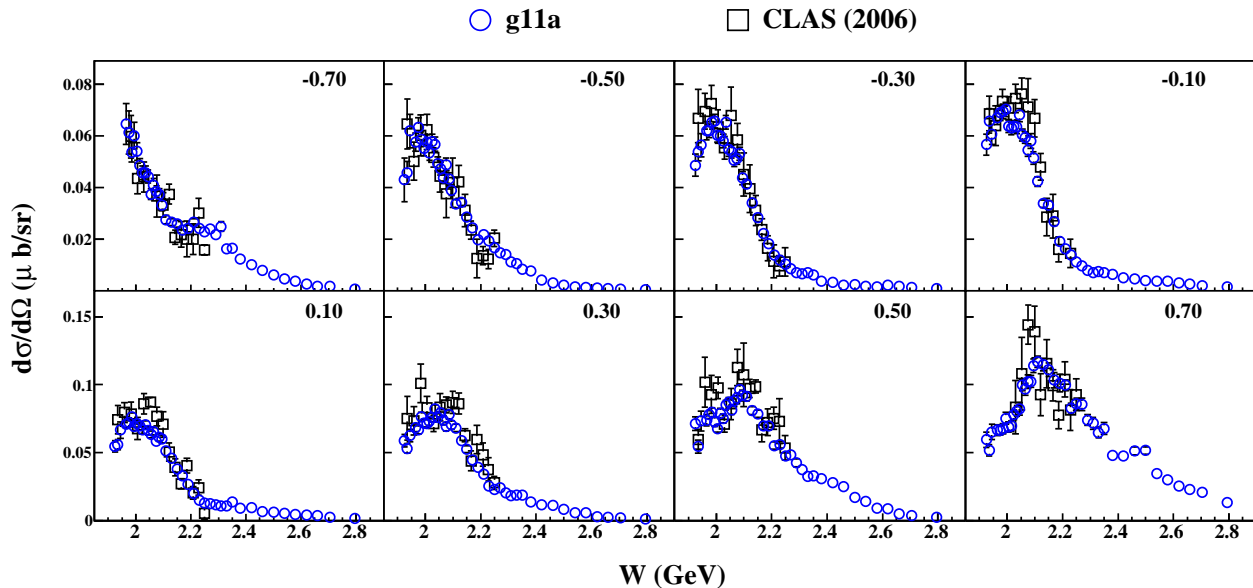


FIG. 9: (Color Online) $\frac{d\sigma}{d\Omega}(\mu\text{b/sr})$ vs. W (GeV) for the $\gamma p \rightarrow p\eta'$ reaction, in $\cos\theta'_{c.m.}$ bins, from previous CLAS data [5] (open squares) and this work (blue open circles). For this comparison, our results were merged into 10 $\cos\theta'_{c.m.}$ bins, eight of which exactly overlap the earlier CLAS measurements shown here (see text for details). The centroid in $\cos\theta'_{c.m.}$ of each bin is labeled on the plot.

Lett. **94**, 012004 (2005).

- [3] F. Renard *et al.*, Phys. Lett. **B528**, 215 (2002).
- [4] T. Nakabayashi, *et al.*, Phys. Rev. **C74**, 035202 (2006).
- [5] M. Dugger *et al.* [CLAS Collaboration], Phys. Rev. Lett. **96**, 062001 (2006).
- [6] A. V. Anisovich *et al.*, Eur. Phys. J. A **25**, 427 (2005).
- [7] D.I. Sober *et al.*, Nucl. Instrum. Methods **A440**, 263 (2000).
- [8] B. A. Mecking *et al.* [CLAS Collaboration], Nucl. Instrum. Methods **A503**, 513 (2003).
- [9] G. Feldman and R. Cousins, Phys. Rev. D **57**, 3873 (1998).
- [10] M. Williams, Ph.D. Thesis, Carnegie Mellon University, 2007, www.jlab.org/Hall-B/general/clas_thesis.html.
- [11] M. Williams, M. Bellis and C. A. Meyer, JINST **4**, P10003, (2009).
- [12] M. Williams *et al.* [CLAS collaboration], submitted to Phys. Rev. C, (2009), arXiv:0908.2910 [nucl-ex].
- [13] M. Williams, Comp. Phys. Comm. **180**, 1847, (2009).
- [14] J. Ball and E. Pasyuk. CLAS Note 2005-002 (2005), www1.jlab.org/ul/Physics/Hall-B/clas/index.cfm.
- [15] Electronic versions of the cross section data presented in this paper can be found online at clasweb.jlab.org/physicsdb.
- [16] K. Nakayama and H. Habermann, Phys. Rev. C **73**, 045211 (2006).
- [17] R.A. Arndt, W.J. Briscoe, M.W. Paris, I.I. Strakovsky, and R.L. Workman, in progress; gwdac.phys.gwu.edu.
- [18] M. McCracken, Ph.D. Thesis, Carnegie Mellon University, 2008, www.jlab.org/Hall-B/general/clas_thesis.html.
- [19] Z. Krahn, Ph.D. Thesis, Carnegie Mellon University, 2007, www.jlab.org/Hall-B/general/clas_thesis.html.
- [20] M. Williams *et al.* [CLAS collaboration], submitted to Phys. Rev. C (2009), arXiv:0909.2911 [nucl-ex].

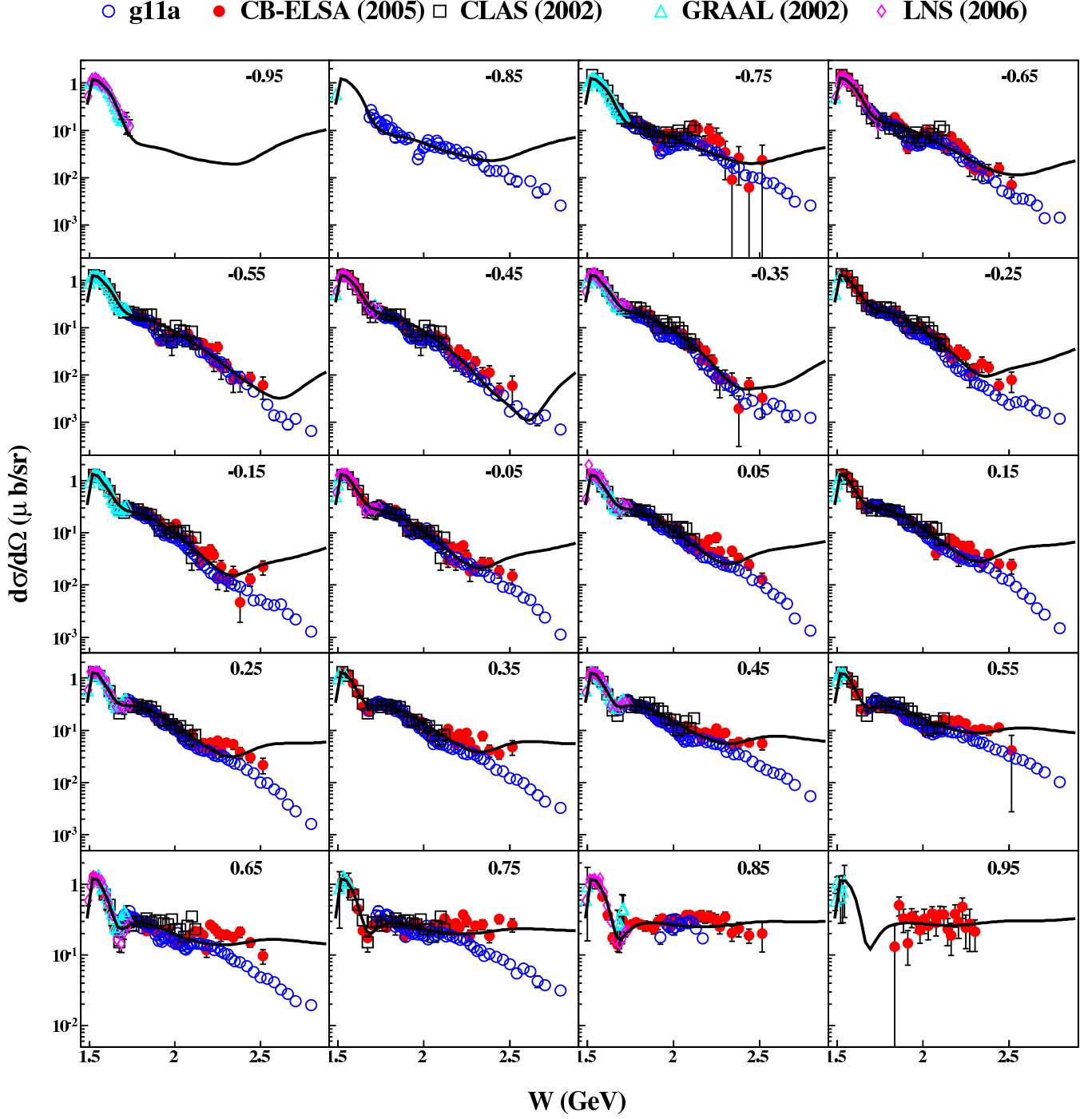


FIG. 10: (Color Online) $\frac{d\sigma}{d\Omega} (\mu\text{b/sr})$ vs. W (GeV) for the $\gamma p \rightarrow p\eta$ reaction, in $\cos\theta_{c.m.}^{\eta}$ bins, from CB-ELSA [2](red filled circles), previous CLAS data [1](open squares), GRAAL [3](light-blue open triangles), LNS [4](purple open diamonds) and this work (blue open circles). The centroid of each bin in $\cos\theta_{c.m.}^{\eta}$ is labeled on each plot. The solid line is a SAID [17] fit to the earlier data.

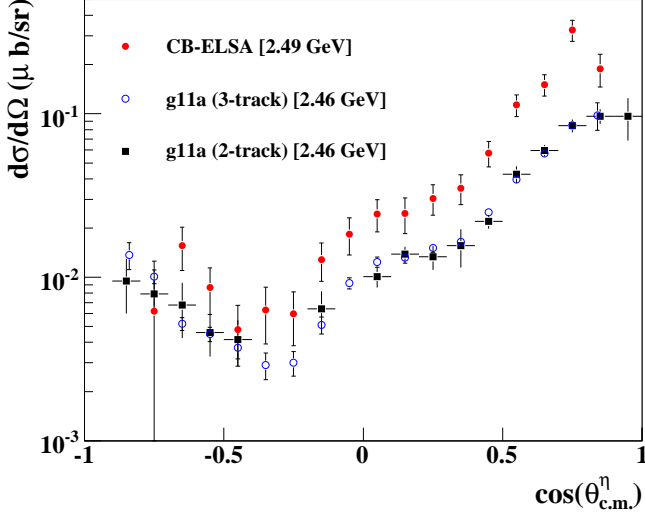


FIG. 11: (Color Online) $\frac{d\sigma}{d\Omega}$ ($\mu\text{b}/\text{sr}$) vs. $\cos\theta_{c.m.}^\eta$: for the reaction $\gamma p \rightarrow p\eta$. Differential cross sections near $W = 2.46$ GeV from CB-ELSA [2] (red filled circles) and from CLAS. The CLAS *g11a* results presented in this work, which required detection of $p\pi^+\pi^-$ (blue open circles), and the “two-track” results discussed in the text, which only required the $p\pi^+$ to be detected (black filled squares) are in excellent agreement. The background levels in the “two-track” topology were too high to permit a reliable extraction of the signal yield for $-0.4 < \cos\theta_{c.m.}^\eta < -0.2$. The “two-track” error bars are purely statistical and do not contain any systematic uncertainty estimates on the signal-background separation.